

## Green hydrogen production from thermoelectric condensation of ambient moist air

Hilal Ahmad<sup>a</sup>, Taqi Ahmad Cheema<sup>a,\*</sup>, Hadeed Ahmed Sher<sup>b</sup>, Cheol Woo Park<sup>c,\*\*</sup>

<sup>a</sup> Faculty of Mechanical Engineering, Ghulam Ishaq Khan Institute of Engineering Sciences and Technology, Topi, 23640, Pakistan

<sup>b</sup> Faculty of Electrical Engineering, Ghulam Ishaq Khan Institute of Engineering Sciences and Technology, Topi, 23640, Pakistan

<sup>c</sup> School of Mechanical Engineering, Kyungpook National University, 80 Daehak-Ro, Buk-Gu, Daegu, 41566, South Korea

### ARTICLE INFO

Handling Editor: Ibrahim Dincer

**Keywords:**

TEWC  
AWE  
Ambient Humidified air  
Numerical modelling  
Multiphysics coupling

### ABSTRACT

As the world transitions towards reducing carbon emissions, green hydrogen produced through solar-powered alkaline water electrolysis (AWE) presents a promising eco-friendly fuel option. In response to the challenges caused by global warming, including air moisture saturation leading to unbalanced rainfall, flooding, concern for freshwater depletion and the limited availability of water and energy sources in arid regions. The present study introduces a novel method of integrating thermoelectric water condenser (TEWC) and AWE for green hydrogen production in remote and arid regions where both the water and the conventional energy sources are scarce. Numerical simulations of the present study show that the impact of relative humidity, temperature, and air flow rate significantly affect water condensation, energy requirement, and hydrogen production. The TEWC and AWE models showed excellent agreement with the experimental data. TEWC model revealed that the highest water production rate of  $1.50 \text{ kg}/(\text{m}^2\text{h})$  is achieved at ambient air temperature of 308 K and relative humidity of 80%. Furthermore, increasing the moist air flow from 1 m/s to 2 m/s results in a 47.5% increase in water production rate. The AWE model showed that cell's performance improved with higher temperatures, lower electrode-separator gap, and overpotentials. The hydrogen evolution rate reached a maximum of  $5.2 \text{ kg}/(\text{m}^2\text{h})$  at current density of  $1.4 \text{ A}/\text{cm}^2$  and potential of 3.96 V. By optimizing the TEWC and AWE systems the integrated method proved to be an efficient way of converting moist air into green hydrogen using solar energy, making it a viable and sustainable setup in remote arid regions.

### 1. Introduction

The interest in developing a sustainable energy future free of carbon emissions has triggered interest in green hydrogen as a clean and versatile energy option [1]. Green hydrogen, produced using renewable sources such as solar and wind power, holds immense potential as a clean energy carrier, mitigating greenhouse gas emissions and addressing the global climate crisis [2]. However, the challenge lies in its production, particularly in arid regions with restricted water supplies [3]. Researchers have explored various techniques for generating potable water, with atmospheric water generation emerging as a promising approach. Moist air condensation using solar-powered Peltier modules presents a sustainable and cost-effective water resource [4]. For instance, Liu et al. [5] investigated a portable water generator that relies on thermoelectric principles. This research showed that water

generation increased with higher relative humidity and airflow rate. The maximum water production rate obtained was  $0.116 \text{ kg}/(\text{m}^2\text{h})$  with a power input of 58.2 W. Challenges such as limited cooling capacity, surface area, and droplet adhesion hindered condensation efficiency. Nevertheless, the system demonstrated energy-saving potential when powered by a Photo-voltaic panel. To enhance efficiency by optimizing heat extraction from the hot side, quantified through coefficient of performance assessments across varied operating conditions. Summers and Asiabaniour [6] investigate different types of cooling methods for a thermoelectric water generator. These methods involve connecting a heat conducting aluminum heat sink, using fans for convective cooling and filling copper heat pipes with water allowing phase change conduction. Sanaye et al. [7] suggested a new thermoelectric approach for sustainable water collecting from air. The group experimentally and through numerical simulations assessed its performance. By coupling the TEC with heat exchangers on the hot side of are capable of achieving

\* Corresponding author.

\*\* Corresponding author.

E-mail addresses: [tacheema@giki.edu.pk](mailto:tacheema@giki.edu.pk) (T.A. Cheema), [chwoopark@knu.ac.kr](mailto:chwoopark@knu.ac.kr) (C.W. Park).

<https://doi.org/10.1016/j.ijhydene.2024.10.126>

Received 7 June 2024; Received in revised form 5 October 2024; Accepted 8 October 2024

0360-3199/© 2024 Hydrogen Energy Publications LLC. Published by Elsevier Ltd. All rights are reserved, including those for text and data mining, AI training, and similar technologies.

**Nomenclature**

$u$	velocity in x-direction [m/s]
$v$	velocity in y-direction [m/s]
$C$	water vapor concentration [ $\text{kg}/\text{m}^3$ ]
$p$	pressure [Pa]
$T$	temerature [K]
$D_{AB}$	mass diffusion coefficient [ $\text{m}^2/\text{s}$ ]
$\Delta G$	Gibbs free energy [kJ]
$z$	number of electrons
$F$	Faraday's Constant [C/mol]
$i_{loc}$	Local charge transfers current density [ $\text{A}/\text{m}^2$ ]
$i_o$	Exchange current density [ $\text{A}/\text{m}^2$ ]
$R$	Universal gas constant [ $\text{J}/(\text{mol K})$ ]
$T$	Temperature [K]
$Q$	General current source term [ $\text{A}/\text{m}^3$ ]
$i$	current density vector [ $\text{A}/\text{m}^2$ ]
$\vec{F}_k$	body force [ $\text{N}/\text{m}^3$ ]
$\dot{m}_{gl}$	mass transfer rate of gas transitioning into the liquid phase [ $\text{g}/(\text{m}^3 \text{s})$ ]
$M_g$	molar mass [g/mol]
$F_{BD}$	bubble dispersion force [ $\text{N}/\text{m}^3$ ]
$K_g$	gas phase dispersion factor
$d_b$	diameter of the bubble [m]
$u_{slip}$	slip velocity [m/s]
<b>GREEK SYMBOLS</b>	
$\rho$	density [ $\text{kg}/\text{m}^3$ ]
$\mu$	dynamic viscosity [Pa.s]

$\beta$	volumetric coefficient of expansion [ $\text{K}^{-1}$ ]
$\beta^*$	species coefficient of expansion [ $\text{m}^3/\text{kg}$ ]
$\alpha$	Thermal diffusivity [ $\text{m}^2/\text{s}$ ]
$\eta$	overpotential (Eta) [V]
$\varphi$	Electric potential (phi) [V]
$\sigma$	Electrical conductivity [S/m]
$\alpha_a$	Anodic charge transfer coefficient [dimensionless]
$\alpha_c$	Cathodic charge transfer coefficient [dimensionless]
$\tau$	Stress tensor in [ $\text{N}/\text{m}^3$ ]
$\alpha_k$	Volume fraction of gas phase [dimensionless]
$\alpha_l$	Volume fraction of liquid phase [dimensionless]

**SUBSCRIPT**

a	Anodic
c	Cathodic
g	gas
l	liquid
aq	Aqueous
rev	Reversible
loc	local
g	gas
o	initial
k	gas phase
gl	gas to liquid
eff	effective
b	bubble
BD	bubble dispersion
d	diameter

better system efficiency while also increasing heat exchange efficiency by reusing cooler air exiting, improving both energy consumption and cost per liter over existing systems. Shahrokh and Esmaeili [8] proposed an electric condenser with an air blower for TEC heat removal on the hot side and studied numerically and experimentally the effects of condenser, current flow, and ambient temperature on water production. It was also concluded that water production increases with increasing humidity and current flow, with an optimum value of 1.25A producing 99.66 ml/h of water. John et al [9] studied the potential applications of Peltier modules in enhancing water production from the air. Their gadget can harvest 2 L of water from the atmosphere in a time frame of 12 h, given certain temperature and humidity requirements. This study indicates that integrating thermoelectric coolers with miniaturized atmospheric water generators may offer an affordable and eco-friendly option.

In some cases, the researchers focus on integrating water production systems with renewable energy like solar energy. Shafeian [10] put forward a fresh approach to categorizing technologies and materials used for generating atmospheric water, with an emphasis on utilizing solar energy either independently or in conjunction with other techniques. Their assessment emphasized the significance of movement and maximizing the utilization of solar energy for devices that are practical and efficient. Efse et al. [11] carried out research to investigate how cooling directly affects the performance of the thermoelectric cooler. Moreover, it stated that the condensation rate is directly related to cold surface temperature reduction with a decrease of 11 °C in the cold side temperature of the TEC, leading to a notable 36.8% enhancement in the water production rate. The findings also indicate that the maximum production rate was achieved at the lowest temperature of 273 K, yielding 0.323 kg/(m<sup>2</sup>h). Joshi et al. [12] also studied the factors influencing water generation in thermoelectric condensation. This study analyzed the impact of internal heat dissipation, air circulation speed, moisture levels, and electrical current on the efficiency of the device's

cooler side. Alenezi et al. [13] examined the effects of various factors in real and controlled weather conditions through both numerical simulation and experimental research and discovered that as relative humidity increased, there was a notable increase in water production. Two TEC modules produced 231 ml/8h in real conditions, 405 ml/8h in controlled conditions, and 437 ml/8h through numerical simulation. Eslami et al. [14] studied how to maximize TEC water production by determining the best number of TEC modules and channel length at various temperatures. Moreover, it was found that the best performance is obtained with a COP of 1.9 when utilizing a system with 18 TEC arranged in series and an air flow rate of 702 ml/min, resulting in a value of 1.638e-04 ml/J. As a result, the ideal channel length is calculated to be 1.386 m, with 0.43 ml/min of water extracted from the air using a minimum of 20 W electrical power under specific conditions. Kashiba et al. [15] introduced a device known as solar chimney, a structure comprising a greenhouse topped with a tall chimney that harnesses the upward movement of hot air. It combines a greenhouse, chimney, and cyclone separator to generate water and electricity. The findings of the study indicated that a 500 m tall solar cyclone could potentially supply water and 75% of electricity needs of 10,000 people in arid regions, but its efficiency requires further research. Similarly, Wu et al. [16] presented a mathematical model of modified solar chimney known as aerological accelerator to extract water and energy from air using a tall tower. The mathematical model was developed to investigate the potential of water and energy generation in various environments. The results suggest that water production rate substantially increased with increasing chimney height and RH.

One promising approach involves integrating TEC water condensers with alkaline water electrolysis to enable green hydrogen production in arid regions, reducing reliance on conventional water sources and promoting a sustainable energy transition. Several recent studies have focused on alkaline electrolysis, for instance Jang et al. [17] studied the temperature's influence on stack efficiency and found out that stack

efficiency and overall cell performance improve with temperature. At 80 °C, heater power consumption decreases with lower current density, while at 0.06 mA/cm<sup>2</sup>, the system and stack efficiencies peak at 81.81% and 78.56%, respectively. Bideau et al. [18] proposes a multi-physics model with description of bubble transfer, enabling good agreement with experimental velocity profiles through the incorporation of a bubble dispersion force. One area of research in AWE involves understanding hydrogen bubble behavior. Wong et al. [19] examined this phenomenon within a single serpentine flow channel of a zero-gap electrolyzer using a 3D CFD transient model. The study identifies three flow regimes, analyzes bubble slug formation, and evaluates influences on flow dynamics and pressure stability, especially around squared and rounded bends. Brauns et al. [20] compared diaphragms and membranes for their performance in alkaline water electrolysis by investigating the ohmic cell resistances and product gas impurities of different materials, specifically focusing on the influence of separators on electrolyte conductivity and material properties. Niroula et al. [21] developed a mathematical model incorporating thermodynamic, electrochemical, and empirical equations and validated it using polarization curve data. Results indicate that higher operational temperature and lower operational pressure reduce electrolysis cell voltage, with 30 wt% KOH solution showing optimal performance compared to other concentrations. Lee et al. [22] developed a 3D transient model featuring a zero-gap configuration and a porous separator, to analyze the electrochemical reactions and transport phenomena that occur during the process. Validation with experiment showed that activation overpotentials dominant at low densities and ohmic loss at high densities, with minimal impact from OH<sup>-</sup> diffusion across separator due to high electrolyte flow rates. Rodríguez and Amores [23] experimentally investigated optimizing electrolyzer parameters of electrode/diaphragm distance variation and electrolyte concentration and validated that high temperature, small electrode spacing, and concentrated electrolytes improved the overall performance, aligning with experimental trends. Zarghami et al. [24] predicted and validated the fluid dynamics of gas and liquid within an electrolyzer. The model incorporated the forces of drag and turbulent dispersion and found that turbulent dispersion force plays a significant role in accurately simulating gas-liquid flow. Barco-Burgos et al. [25] evaluated the impact of current conditions and electrode distance on hydrogen production efficiency, with optimal performance achieved at a 3 mm electrode separation and 30 A current at 12 V. Maximum efficiencies of 4.6% for the cell and 31% were achieved for the entire system. Lopata et al. [26] experimentally validated a 3D CFD model and efficiently determined temperature and current distributions in a PEMWE device, offering an efficient method for evaluating the performance of cell at high feed rates and facilitating large stacks of temperature management. With low error observed at flow rates above 0.6 ml/(min.cm<sup>2</sup>), the model enables pre-determination of anode temperature, aiding in temperature management to mitigate unfavorably high local temperatures. Abdelsalam et al. [27] investigated the feasibility of using Solar Chimney Power Plants (SCPPs) to produce green hydrogen. They analyzed the potential of SCPPs to generate electricity, distilled water, and hydrogen, considering factors such as solar radiation, temperature, and economic viability. The results showed that SCPPs could be a promising solution for storing and utilizing excess renewable energy, with potential economic benefits and environmental advantages. Nevertheless, Abdelsalam et al. [28] in this study investigated a novel hybrid solar chimney power plant (HSCPP) coupled with a water-splitting process. The HSCPP can produce desalinated water, green hydrogen, and electrical energy. The system utilizes solar energy to heat air, drive a turbine, and produce electricity. Electricity is used to electrolyze water, generating hydrogen and oxygen. The study found that the HSCPP has a high efficiency for hydrogen production and can produce significant amounts of desalinated water. These results suggest that HSCPP could be a promising sustainable solution for producing green hydrogen and water. Integration of membrane distillation with electrolysis is also a feasible solution.

For this purpose, Arthur et al. [29] investigated the potential benefits of integrating membrane distillation (MD) into a water electrolysis system. The MD process could use waste heat from the electrolysis to desalinate feedwater, reducing the need for a separate heat exchanger and providing purified water for the electrolyzer. The results showed that the MD system successfully produced high-quality water for use in electrolysis, with a water flux of 5 L/m<sup>2</sup>/h and a recovery rate of 0.1%. Future research should focus on evaluating the economic and operational benefits of replacing the traditional heat exchanger with an MD heat exchanger. Moreover, Harada et al. [30] studied a techno-economic analysis of an integrated system for carbon capture and utilization (CCU). The system captures CO<sub>2</sub> from the air using a DAC process and converts it into synthetic natural gas (SNG) using hydrogen from water electrolysis. The analysis uses mathematical models to estimate energy consumption, capital costs, and operating costs. The results indicate that the cost of SNG produced by this system is within the range of 1.43–2.60 \$/Nm<sup>3</sup>-SNG. Similarly, Modestino et al. [31] investigated a novel microfluidic platform for water-splitting using humid air. The platform uses polymeric ion-conductor thin films to absorb water from the air and enable the electrochemical process. The study found that the device performance is influenced by factors such as Nafion film thickness, air convection, and water content in the ionomer. The results provide insights for designing practical electrochemical hydrogen generators that operate directly with ambient air.

Previous research studies, such as Guo et al. [3] and Cattani et al. [4], mostly focused on the production of atmospheric water using different techniques, such as direct air electrolysis and air water generator. Guo et al. [3] presented a new device Direct Air Electrolysis, that can produce hydrogen directly from air moisture by sandwiching hygroscopic electrolyte in sponge, eliminating reliance on fresh water. The prototype operates in a dry environment and integrates with renewables, achieving continuous hydrogen production. This gives an idea for sustainable hydrogen generation in arid regions. Based on water quality necessary for electrolysis Cattani et al. [4] explore AWG to overcome water limitations in green hydrogen production. It investigates water quality and energy usage of AWGs for electrolysis. The results suggest AWGs are a feasible solution due to their ability to produce high pure water while achieving sufficient energy efficiency. Most of the above studies provided data about the TEC moisture condensation and AWE separately. Few studies, such as Direct Air Electrolysis proposed by Guo et al. [3] and Air Water Generator by Cattani et al. [4], have reported on developing combined devices that integrate water production and hydrogen generation from atmospheric air. Their studies are among the limited examples in the literature that explore this combined approach, serving as key references that demonstrate the feasibility of such integrated systems. Climate change has increased atmospheric moisture, causing erratic rainfall and flooding. Meanwhile, freshwater scarcity is a big concern, especially in arid regions. Therefore, the present study introduces a novel method of integrating TEWC and AWE for green hydrogen production in remote and arid regions where both the water and the conventional energy sources are scarce. The system helps the environment by condensing atmospheric moisture while preserving limited freshwater resources. However, to the best of the author's knowledge, no study has reported the use of integrated TEC-based atmospheric water extraction with the AWE process for developing a sustainable, solar-powered system of green hydrogen production in remote arid regions. This system uniquely addresses the dual challenges of water scarcity and energy supply by utilizing atmospheric moisture and solar energy, ensuring renewable and continuous water sources for green hydrogen production through an efficient AWE process. The proposed simulation model improves the performance of coupled systems under varying environmental conditions, further highlighting the practicality and feasibility of this approach. This kind of integrated solution will help in progressing toward a green hydrogen economy by having a feasible tool for hydrogen production in demanding environments and promoting sustainability with a reduced dependency on fossil

fuels. Therefore, to cope with the challenges of limited water and conventional energy sources in arid regions, computational analysis is carried out using COMSOL Multiphysics software to investigate the performance of the coupled system. The computational analysis focuses on the Multiphysics aspects, allowing us to optimize the TEC water condenser and AWE by considering the effects of various optimizing parameters, including moist airflow, the temperature of the TEC cold surface, relative humidity, and applied current on TEC water condenser. Concurrently, the impacts of cell voltage, current density, temperature, electrode-diaphragm gap, hydrogen evolution rate, and Polarization curve are investigated on AWE for green hydrogen production.

## 2. Methodology

The numerical modeling and analysis of the integrated system, comprising a thermoelectric water condenser (TEWC) coupled with an alkaline water electrolyzer (AWE), were performed using the COMSOL Multiphysics software. The modeling and numerical analysis of the integrated system consists of two separate systems: TEC water condenser modeling and simulation and AWE modeling and simulation.

### 2.1. Thermoelectric water condenser (TEWC) modeling

The Peltier effect, known as thermoelectric cooling, describes the phenomenon where heat is either absorbed or released as current passes through an interface between two dissimilar semiconductors. A Peltier module consists of numerous thermocouples wired electrically in series but thermally connected in parallel. These thermocouples are sandwiched between  $\text{Al}_2\text{O}_3$  plates. The computational model of TEWC has two domains, the TEC domain, and the moist air domain, as shown in Fig. 1. These are coupled through multiphysics coupling to directly correlate applied current and condensation rate, just like the actual system. The moist air domain consists of a 3D-CAD model, as shown in Fig. 1(b), with dimensions of  $8.5 \text{ cm} \times 8.5 \text{ cm} \times 8 \text{ cm}$ . Meanwhile, the TEC domain consists of a CAD model of 4 TEC1-12706 connected in

series with their default dimensions. 4 TECs were used in series for energy efficiency and increased water condensation as suggested by Alenezi et al. [13]. These TECs were arranged in a series, forming a square shape with a gap between them for connections. This configuration aims to minimize power consumption and cold face temperature and enhance the surface area for cooling and condensation. Current applied in auxiliary sweep ranging from  $0.5 \text{ A}$  to  $2.5 \text{ A}$  to the positive terminal of TECs while the negative terminal is considered ground. A stationary study with a parametric sweep was applied to analyze the temperature of the TEC cold face, while the hot face was applied with a boundary condition of constant temperature for continuous heat removal. In this numerical study, the TECs are simulated separately and then linked through Multiphysics coupling to the moist air domain. The TEC cold face temperature is linked to the moist air domain by assuming only its cold surface as boundary condition for moist air domain. The temperature of ambient moist air is  $308 \text{ K}$ , and the relative humidity is  $80\%$ . Inlet and outlet ports are positioned on opposite sides for the moist air domain to facilitate airflow. Moist air at  $308 \text{ K}$  and  $80\% \text{ RH}$  enter through an inlet at the rate of  $0.5 \text{ m/s}$ , shown in Fig. 1(b). While passing through the cold surface, the cold surface absorbs heat from the moist air, initiating air cooling. As the air moves through the chamber, its temperature decreases until it reaches the dew point, leading to condensation. Condensation can be further enhanced by hydrophobicity of cold surfaces that can reduce wettability, leading to larger, more spherical droplets that roll off easily compared to hydrophilic surfaces. This increased droplet mobility improves water removal, thereby boosting the overall condensation rate and enhancing heat transfer performance Jain et al. [37]. In a stationary study, the moist air physics combined laminar flow, heat, and mass transport.

#### 2.1.1. Governing equations for TEWC

The governing equations for the moist air condensation through thermoelectric coolers, was incorporated into the model through the following equations [11,33]:

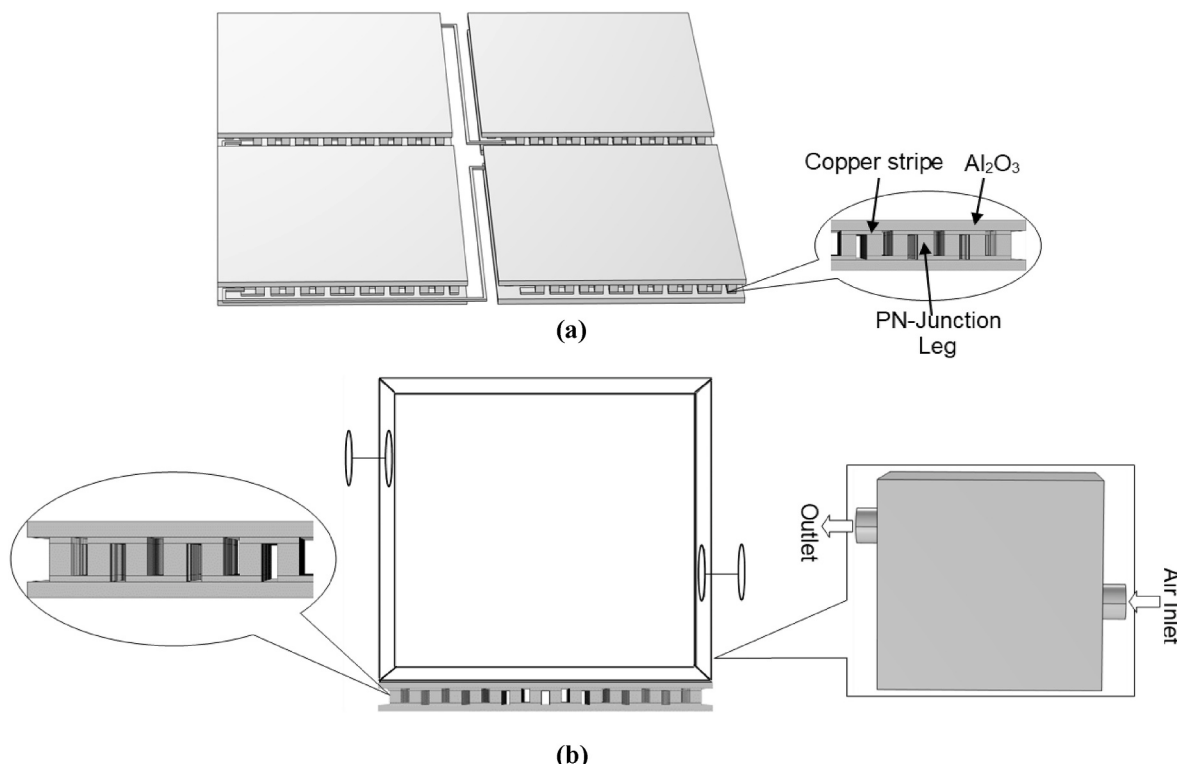


**Fig. 1.** Computational Model for TEWC with (a) Computational Model for TEC (b) Computational Model for Moist air Domain.

$$\frac{\partial u}{\partial x} + \frac{\partial v}{\partial y} = 0 \quad (1)$$

$$\rho \left[ u \frac{\partial u}{\partial x} + v \frac{\partial u}{\partial y} \right] = - \frac{\partial p}{\partial x} + \mu \left[ \frac{\partial^2 u}{\partial x^2} + \frac{\partial^2 u}{\partial y^2} \right] \quad (2)$$

$$\rho \left[ u \frac{\partial v}{\partial x} + v \frac{\partial v}{\partial y} \right] = - \frac{\partial p}{\partial y} + \mu \left[ \frac{\partial^2 v}{\partial x^2} + \frac{\partial^2 v}{\partial y^2} \right] + \beta g(T - T_0) + \beta^* g(C - C_0) \quad (3)$$

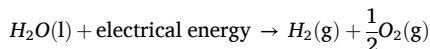
$$u \frac{\partial T}{\partial x} + v \frac{\partial T}{\partial y} = \alpha \left[ \frac{\partial^2 T}{\partial x^2} + \frac{\partial^2 T}{\partial y^2} \right] \quad (4)$$

$$u \frac{\partial C}{\partial x} + v \frac{\partial C}{\partial y} = D_{AB} \left[ \frac{\partial^2 C}{\partial x^2} + \frac{\partial^2 C}{\partial y^2} \right] \quad (5)$$

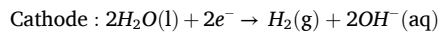
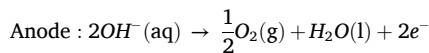
In these equations,  $v$ ,  $u$ ,  $C$ ,  $p$ ,  $T$  and represent the velocity x-axis and y-axis components, water vapor concentration, pressure, and temperature respectively. The symbols  $D_{AB}$ ,  $\beta$ , and  $\beta^*$  denote mass diffusion coefficient, expansion coefficient (volumetric), and expansion coefficient (species) respectively.

## 2.2. Alkaline water electrolyzer (AWE) modeling

AWE stands as a well-established method for generating hydrogen gas by splitting water molecules through electrochemical splitting. This process involves an electric current that is passed through a KOH solution, which acts as a conductor. At the cathode, water undergoes a reduction reaction, splitting into hydrogen gas and hydroxide ions. At the anode, water molecules undergo oxidation, releasing oxygen gas. The overall reaction for water splitting is as follow [32,36]:



While the cathodic and anodic half-cell reactions are [32,36]:



The complete reaction for water splitting requires a minimum electric voltage (reversible voltage) across the two electrodes. The minimum electric voltage, also termed as reversible voltage, is determined based on the Gibbs energy for water splitting [23]:

$$\Delta G = zF U_{rev} \quad (6)$$

$$U_{rev} = \frac{\Delta G}{zF} \quad (7)$$

$$U_{rev} = \frac{\left( 237.2 \frac{kJ}{Kmole} \right)}{\left( 2 * 96485 \frac{C}{mole} \right)} = 1.229 V \quad (8)$$

$\Delta G$  = Gibbs Energy,  $F$  = Faraday's Constant,  $z$  = numbers of electron.

The minimum or the reversible voltage is equal to 1.229 V at STP (298 K and 1 bar). This value, consistent with the second law of thermodynamics, is  $\Delta g^0 = 273.2 \text{ kJ/mol}$ .

However, the actual cell voltage ( $U$ ) always exceeds the reversible voltage because of irreversibility or overpotentials. Consequently, the actual cell voltage is defined as the sum of the reversible voltage ( $U_{rev}$ ) and the overpotentials ( $\eta$ ), as shown in Equation [9].

$$U = U_{rev} + \sum \eta \quad (9)$$

The  $\sum \eta$  term represents the sum of ohmic, activation, and concentration overpotentials, each defined as follows [23]:

- Activation overpotentials: Activation overpotentials arise due to the energy barriers that need to be overcome for hydrogen and oxygen to form on the electrode surfaces.
- The total electrical resistance includes contributions from various components: the electrodes themselves, current collectors, and the resistance associated with transporting ions through the electrolyte, gas bubbles within the cell, and the diaphragm's resistivity.
- Concentration overpotentials: Arising from mass-transport restrictions encountered at the electrode surfaces during high-current conditions.

These overpotentials influence the cell voltage ( $U$ ). Their effect can be visualized through the polarization curve of an electrolysis cell, as shown in Fig. 2.

### 2.2.1. AWE cell geometry

Fig. 3(a) illustrates the 2D geometric representation of an AWE cell, which is based on commercial AWE designs. The 2D geometry approximation was adopted to simplify the model and reduce complexity and enable a focused examination of the primary variables involved. The AWE setup comprises of two compartments, one cathodic (3 mm) and the other anodic (3 mm), separated by a diaphragm/separators (1 mm) as mentioned in Table 1. The separator acts as a barrier, preventing the produced hydrogen and oxygen gases from mixing. It also helps maintain low electrical resistance within the cell. Both the anode and cathode compartments are filled with an electrolyte solution, usually aqueous (KOH). Within these compartments, the cathode and anode electrodes are positioned on opposing walls. At cathode hydrogen gas ( $H_2$ ) is liberated, while oxygen gas ( $O_2$ ) is liberated at the anode. The electrodes, 100 mm in height, were characterized by two basic boundary conditions labelled in Fig. 3(a) on either side of the cell, functioning as current collectors. A velocity-inlet boundary condition of  $u = 1.5 \text{ m/s}$  with a uniform velocity profile is used for the electrolyte flow rate within the computational domain. The inlet boundary is set at the bottom lines of the two compartments, and the outlet boundary is at the top lines as shown in Fig. 3 (a). To minimize any upstream effects of the outlet boundary condition on fluid flow, the height of the cell is set to 10 cm, making the total computational domain height 10 cm. All other boundaries are treated as no-slip boundaries.

### 2.2.2. Numerical model

The COMSOL Electrolyzer Module, used for simulating the AWE

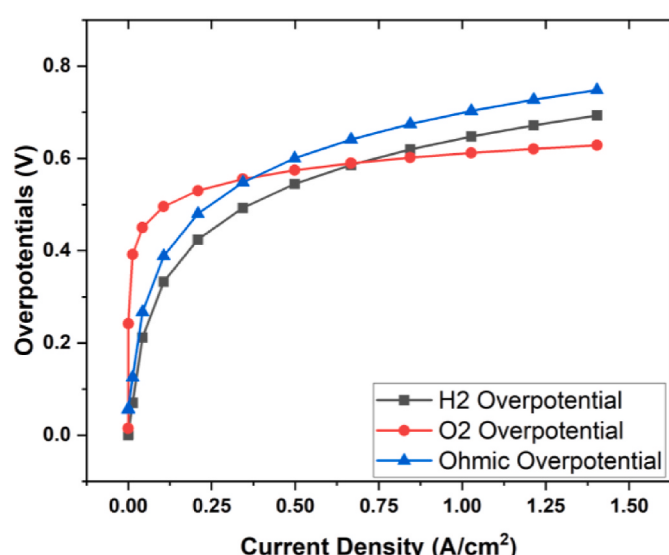


Fig. 2. Visual presentation of I-V characteristics with contribution of each overpotentials.

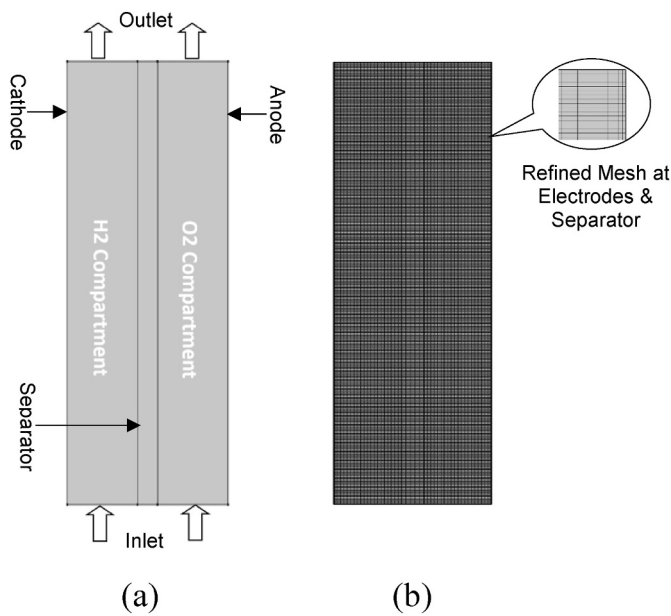


Fig. 3. (a) Computational model of AWE (b) Meshing of AWE.

**Table 1**  
AWE model specification.

Parameter	Value	Unit
Electrode height	100	mm
Cell Width	7	mm
Separator	1	mm
H <sub>2</sub> & O <sub>2</sub> compartment width	3	mm

model, comprises two interfaces. Water Electrolyzer interface and Laminar flow interface. The Laminar flow interface is defined by adding default material, Aqueous Alkali, which consider the inlet flow rate as an aqueous (Aq) solution of KOH. The concentration of this Aq KOH depends on molality parameter given in Table 2. Which automatically incorporates the characteristics of Aq KOH and necessary alkalinity for efficient electrolysis process. The output from the TEWC is linked directly to the AWE system as a single flow rate input. This input flow rate is considered by the Laminar flow interface as the flow rate of the Aq

**Table 2**  
2D AWE model parameters.

Symbol	Value	Description
T	343.15 K	Operating temperature
P <sub>g</sub>	1.0133E5 Pa	Gas pressure
P <sub>v</sub>	31201 Pa	Vapor pressure
xH <sub>2</sub> O(P <sub>v</sub> /P <sub>g</sub> )	0.30793	molar fraction (water) in gas phase
xH <sub>2</sub> (1-xH <sub>2</sub> O)	0.69207	molar fraction (H <sub>2</sub> ) in gas phase
xO <sub>2</sub> (1-xH <sub>2</sub> O)	0.69207	molar fraction (O <sub>2</sub> ) in gas phase
d <sub>b</sub>	1e-4 m	Bubble diameter
$\alpha_a$	0.6	Anodic charge transfer coefficient
$\alpha_c$	0.77	Cathodic charge transfer coefficient
v_in_H <sub>2</sub>	1.5 m/s	Average flow, hydrogen side
v_in_O <sub>2</sub>	1.5 m/s	Average flow, oxygen side
I <sub>o_ref</sub> H <sub>2</sub>	90 A/m <sup>2</sup>	H <sub>2</sub> exchange current density
I <sub>o_ref</sub> O <sub>2</sub>	0.5 A/m <sup>2</sup>	O <sub>2</sub> exchange current density
MH <sub>2</sub> O	0.018 kg/mol	molar mass of water
MO <sub>2</sub>	0.032 kg/mol	molar mass O <sub>2</sub>
MH <sub>2</sub>	0.002 kg/mol	molar mass H <sub>2</sub>
MOH	0.017 kg/mol	molar mass OH
Eps-gap	0.3	Separator porosity
c-KOH	6000 mol/m <sup>3</sup>	Electrolyte concentration
E-cell	1.2 V	Cell voltage
F	96,485.3 C/mol	Faraday constant

KOH as discussed above. Thus, the two models can be coupled using Multiphysics through this approach as shown by coupling flowchart in Fig. 4. As mentioned previously this study numerically simulate the electrochemical and fluidic behavior within an AWE. The numerical model incorporated an electrochemical component to simulate the water electrolysis process and calculate the current distribution, enabling the generation of polarization curves. To analyze the production and distribution patterns of hydrogen and oxygen gases within the compartments, the “Euler-Euler Laminar flow” module was employed. Numerical study was performed under steady-state conditions, providing insights into the gas flow dynamics within the electrolyzer. The model incorporates the following assumptions:

- Fluid Properties: The model treated both the gas and electrolyte phases as Newtonian fluids, accounting for their viscous and incompressible nature.
- Constant Properties: Material properties are assumed to remain constant throughout the simulation.
- Shared Pressure Field: The pressure field is assumed to be identical for both gas and electrolyte phases.
- Uniform Electrolyte: Due to efficient ion distribution, the electrolyte is considered uniformly distributed with minimal impact on the results.
- Isothermal Flow: Heat transfer is neglected, simplifying the model to isothermal flow.
- Species Crossover: H<sub>2</sub> and O<sub>2</sub> crossover through the separator is negligible.
- Bubble Size: Bubbles are assumed to maintain a constant diameter at a given current density, with no merging or break-up occurring.
- Turbulent Dispersion: Bubble-bubble interaction is accounted for through the incorporation of dispersion force.
- Laminar Flow: Flow is considered as laminar.

#### 2.2.3. Numerical simulation methodology

The TEWC and AWE models begin with New Model Wizard, where a 3D geometry of the TEWC and 2D geometry of AWE were constructed. The physics modeling of TEWC involves defining heat transfer, laminar flow, and moisture transport in moist air, capturing the thermophysical properties of the materials involved. Whereas the Electrolyzer Module simulates the electrochemical reactions. The Euler-Euler multiphase laminar flow captures the interaction between the electrolyte and the produced gases. The simulation calculates the hydrogen production rate, current efficiency, and flow dynamics, helping optimize the integrated system for green hydrogen production. Boundary conditions are then applied, particularly focusing on temperature, fluid flow, electric potential and mass transfer rates. The model is meshed and optimized to ensure accurate resolution, followed by the selection of a time-dependent study to simulate transient behavior in moisture condensation. Finally, the results are extracted and post-processed, analyzing the water condensation rate, which is essential for further coupling along with I-V characteristics, and hydrogen production rate.

Once the water condensation rate from the TEWC simulation is obtained, this value is used as an input boundary condition in the AWE model. Specifically, the water yield serves as the inlet flow rate in the Laminar Flow Physics of the Electrolyzer module. The AWE model simulates the electrochemical reactions and hydrogen production based on the flow rate of water provided from the TEWC system. By coupling these two systems through the water flow rate, the overall system simulates hydrogen production under realistic conditions where water is generated from air moisture and fed directly into the electrolysis process.

#### 2.2.4. Secondary current distribution and governing equations

A secondary current distribution model was used in this work to capture the electrical properties of the AWE. This simulation method, which was based on the Butler-Volmer equation, Ohm's law, and current

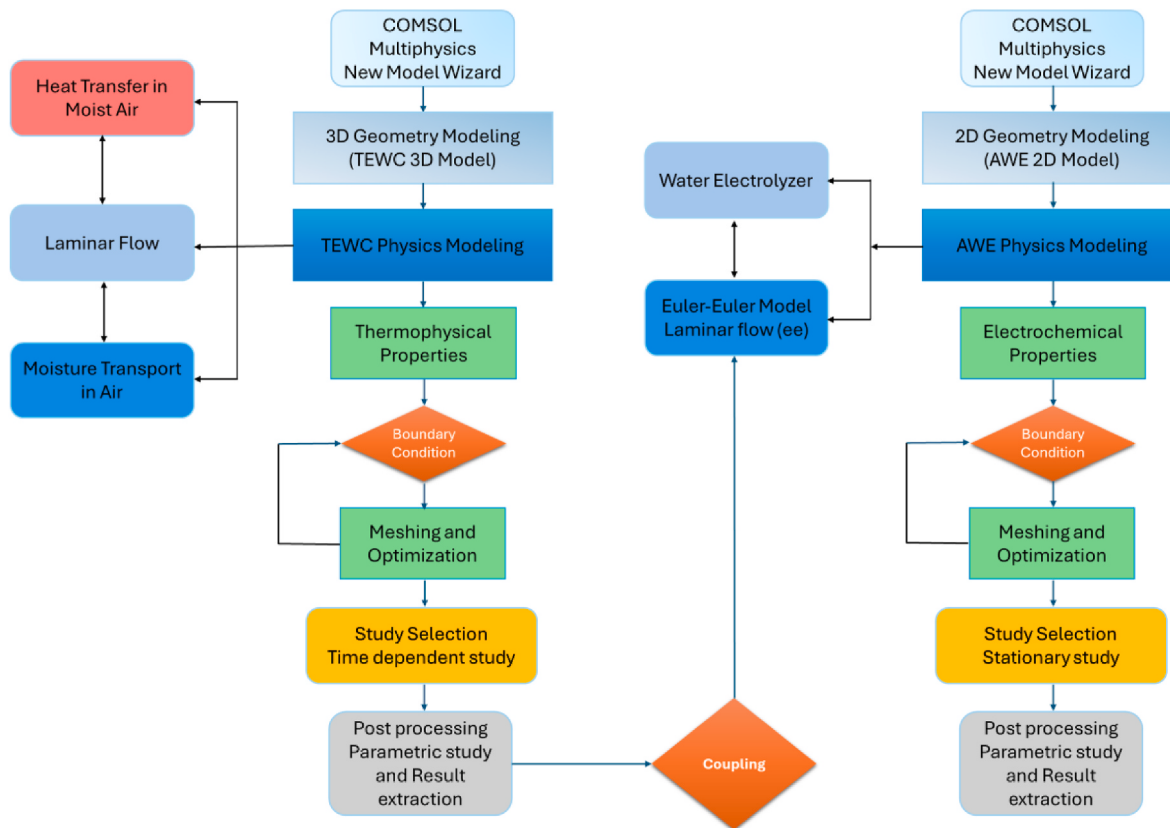


**Fig. 4.** Multiphysics coupling flowchart of the TEWC and AWE simulation model.

conservation, was used to calculate the total potential. The effect of electrode kinetics and current density distribution on the electrochemical process were computed using these governing equations. Equation (10) is used to calculate the total potential of the cell. These governing equations are given below:

$$U_{\text{Cell}} = U_{\text{rev}} + \eta_{\text{ohm}} + \eta_{\text{act,a}}(i) + \eta_{\text{act,c}}(i) \quad (10)$$

$$i_{\text{loc}} = i_{\text{o}} \left[ \exp\left(\frac{\alpha_a F \eta z}{RT}\right) - \exp\left(-\frac{(1-\alpha_a) F \eta z}{RT}\right) \right] \quad (11)$$

$$Q = \nabla \cdot i \quad (12)$$

$$i = -\sigma \nabla \varphi \quad (13)$$

$U_{\text{rev}}$ : Reversible voltage (V),  $\eta_{\text{ohm}}$ : Ohmic overpotential (V),  $\eta_{\text{act,a}}(i)$ : Activation overpotential at anode (V),  $\eta_{\text{act,c}}(i)$ : Activation overpotential at cathode (V),  $i_{\text{loc}}$ : Local charge transfer current density ( $\text{A}/\text{m}^2$ ),  $i_{\text{o}}$ : Exchange current density ( $\text{A}/\text{m}^2$ ),  $\alpha_a$ : Anodic charge transfer coefficient,  $\alpha_c$ : Cathodic charge transfer coefficient,  $\eta$ : Activation overpotential (V),  $F$ : Faraday constant ( $\text{C}/\text{mol}$ ), and  $R$ : Universal gas constant ( $\text{J}/\text{mol}^* \text{K}$ ),  $Q$ : General current source term ( $\text{A}/\text{m}^3$ ),  $i$ : Current density vector ( $\text{A}/\text{m}^2$ ),  $\varphi$ : Electrical potential (V),  $\sigma$ : Conductivity ( $\text{S}/\text{m}$ ).

The Euler-Euler model is employed to represent the behavior of two-phase flow. This model calculates the void fraction of each phase without detailing individual bubbles. Each phase is characterized by its own velocity field, with the dynamics governed by the continuity equation (14) and momentum equation (15) [33,34].

$$\frac{\partial}{\partial t} (\alpha_g \rho_g + \alpha_l \rho_l) + \nabla \cdot (\alpha_g \rho_g \vec{u}_g + \alpha_l \rho_l \vec{u}_l) = 0 \quad (14)$$

$$\frac{\partial}{\partial t} \left( \rho_k \alpha_k \vec{u}_k \right) + \nabla \cdot \left( \rho_k \alpha_k \vec{u}_k \vec{u}_k \right) = \alpha_k \rho_k \vec{g} - \alpha_k \nabla p + \nabla (\alpha_k \tau_k) + \vec{F}_k \quad (15)$$

In the equations,  $u$  represents the velocity in meters per second,  $p$  denotes the pressure in pascals,  $\alpha$  symbolizes the void fraction,  $\tau$  signifies the stress tensor in  $\text{N}/\text{m}^3$ ,  $\vec{F}_k$  represents the body force in  $\text{N}/\text{m}^3$ , and the subscript  $k$  differentiates between the gas phase and the liquid phase.

One way to analyze the void fraction of gas over time is through a transport equation, given by Equation (16);

$$\frac{\partial \alpha_g \rho_g}{\partial t} + \nabla \cdot (\alpha_g \rho_g \vec{u}_g) = -\dot{m}_{gl} \quad (16)$$

The  $\dot{m}_{gl}$  represents the mass transfer rate of gas transitioning into the liquid phase. This rate is typically measured in  $(\text{g}/\text{m}^3\text{s})$ .

This simplified 2D model assumes the Faraday equation governs the rate of gas generation in  $(\text{g}/\text{m}^3\text{s})$  at the electrode's active surface. Faraday equation is given by:

$$\dot{m}_g = \frac{i \cdot M_g}{nF} \quad (17)$$

Where  $(i)$  represents the current density in amperes per square meter,  $M_g$  denotes the molar mass in grams per mole, and  $n$  symbolizes the number of electrons transferred for the specific gas species ( $\text{H}_2$  or  $\text{O}_2$ ), as indicated by the subscript  $g$ .

### 2.2.5. Effect of bubble

KOH electrolyte conductivity suffers due to gas bubbles. These bubbles act like tiny roadblocks on the electrode surface, hindering ion movement and lowering the rate of charge transfer (exchange current density). Equations (18) and (19) account for this effect by considering effective conductivity and adjusted exchange current density.

$$\sigma_{\text{eff}} = \sigma_o (1 - \alpha_g)^{1.5} \quad (18)$$

$$i_{\text{eff}} = i_o (1 - \alpha_g)^{1.5} \quad (19)$$

The equations introduce  $\sigma_{\text{eff}}$  as the effective electrolyte conductivity in S/m,  $\sigma_0$  representing the total conductivity, and  $i_{\text{eff}}$  and  $i_0$  denoting the effective and total exchange current densities in A/m<sup>2</sup>, respectively. The variable  $\alpha_g$  signifies the gas volume fraction, with the subscript g differentiating between hydrogen (H<sub>2</sub>) and oxygen (O<sub>2</sub>).

The Euler-Euler model accounts for gas bubbles in liquids by adding a force term to the momentum equations. This force depends on liquid density, a bubble dispersion factor, bubble size, and the difference in velocity between the bubbles and the liquid. This term is defined as [35]:

$$F_{BD} = -\phi_d \rho_1 \frac{K_g}{d_b} |u_{\text{slip}}| |\nabla \phi_d| \quad (20)$$

Where  $\rho_1$  represents the density of the liquid phase,  $K_g$  denotes a gas phase dispersion parameter,  $d_b$  stands for the diameter of the bubble, and  $u_{\text{slip}}$  signifies the slip velocity.

### 2.2.6. Meshing

A Physics-controlled mesh with normal setting option and minimum element size of 0.0825 cm was built for TEWC part while User-controlled mapped mesh with Quads elements and minimum size of 1.95e-6 cm with extra refinement near anode, cathode and near both side of separator. Considering the minute bubble dimensions (0.01 cm), the mesh element size was carefully selected as 0.005 cm, with further refinement implemented in the wall proximity regions to precisely capture the steep gradients anticipated in those areas as shown in Fig. 3(b). To ensure accurate solution accuracy, a grid independence study was conducted. Stretched meshes with varying element counts were employed for this purpose. A comparison of results obtained using meshes with 88200 and 49700 elements revealed less than 0.1% difference, indicating negligible grid dependency as shown in Table 3. Consequently, both mesh sizes were deemed suitable for the current analysis.

## 3. Result and discussion

### 3.1. Analysis of TEWC result

The proposed computational analysis of TEWC investigates the impact of various parameters on the moisture condensation rate using TECs. These parameters include current, velocity, RH and TEC cold face temperature discussed here in details:

#### 3.1.1. The impact of current on rate of condensation

The amount of electricity supplied to the TECs significantly influences the rate of condensation in the TEWC. In this study, the cold side of the TECs is used to cool the surface where the moist air condenses, forming liquid water. As the current input to the TECs increases, the temperature difference between the hot and cold sides becomes more significant, leading to a lower temperature of 272 K on the cold side at 1.5 A as shown in Fig. 5(a). This enhanced cooling effect results in a more efficient condensation process, allowing a larger portion of the water vapor present in the moist air to condense into liquid water. Therefore, computational analysis of TEWC reveals coupling of TECs with a condensation model in a Multiphysics simulation allows to explore the effects of supplied current directly on water generation rate. With increased electricity, the colder TEC surface can condense more water vapor from the air, leading to a higher water production rate. Fig. 5(a) shows that TEC cold face temperature approached 272 K

**Table 3**

Mesh dependency test model condition: 343 K, 6 M KOH, and 1.5 m/s.

Number of elements	H <sub>2</sub> Evolution rate (kg/m <sup>2</sup> h)	Error (%)
24500	1.2811	0.04
49700	1.2807	0.01
88200	1.2805	0
124000	1.2805	0

indicating effective Peltier cooling at 1.5 A with hot face temperature of 308 K set as boundary condition for removing heat from hot side in order to keep the cold face temperature constant at 272 K. The normalized condensation rate showed a peak of 0.758 kg/(m<sup>2</sup>h) by reducing cold side temperature from 300 K to 272 K at constant RH and flow rate of 2 m/s as shown in Fig. 5(b).

It is essential to note that there is an optimal range of current input beyond which water generation rate may not increase proportionally. Excessive current input can lead to inefficiencies and potential degradation of the TECs due to increased heat generation and thermal stress.

#### 3.1.2. The impact of relative humidity on rate of condensation

The condensation rate within the TEWC system is significantly influenced by the relative humidity of the inlet air stream, which quantifies the actual water vapor content relative to the maximum moisture-holding capacity of air at the given temperature. When the inlet air has a higher relative humidity, it contains a larger quantity of water vapor molecules. As this moist air passes over the cooled surface of the TECs, the increased water vapor content enhances the condensation rate, resulting in a higher water generation rate. Conversely, if the inlet air has a lower relative humidity, the amount of water vapor available for condensation is limited, leading to a reduced water generation rate. The relative humidity distribution as shown in Fig. 6(a) exhibits a gradient increasing towards the cold plate, reaching a saturated value of 1.0 where air condenses vapor upon contact with the cold surface. Also increasing absolute humidity from 65% to 90% is directly related to condensation rates by increasing the moisture content in the inlet air as shown in Fig. 6(b).

#### 3.1.3. The impact of inlet air mass flow rate on rate of condensation

The mass flow rate or the velocity of the inlet air also plays a very important role in TEWC. A higher inlet velocity of moist air implies that a larger volume of moist air is exposed to the cooled surface of the TECs. When the inlet velocity is increased, more water vapor molecules are brought into contact with the condensation surface, potentially leading to a higher condensation rate. However, it is important to consider that an excessively high mass flow rate may not allow sufficient residence time for the condensation process to occur effectively, ultimately limiting the water generation rate. The velocity contours presented in Fig. 7(a) reveal that changes in the cold plate temperature do not significantly alter the overall flow pattern within the system. However, there is a slight influence on the air velocity magnitudes themselves. However, Fig. 7(a) shows that inlet air velocity distribution demonstrates a uniform flow over the cold surface helping in longer contact of air with cold surface. Fig. 7(b) shows that increasing velocity from 1 m/s to 4 m/s increases the condensation rate leading to a maximum of 1.5 kg/(m<sup>2</sup>h) at constant cold face temperature of 272 K and 80% RH.

#### 3.1.4. The impact of temperature on rate condensation

Fig. 8(a) shows the amount of water condensed (ml/h) against temperature variation of inlet air at the fixed condition of RH 89%. As illustrated in Fig. 8(a), an increase in the inlet air temperature results in a corresponding rise in the rate of condensation. This phenomenon occurs because, at a higher temperature, the water content of the air increases to maximum level. The comparison of the present study with the experimental results of Shahrokh and Esmaili [8] was conducted to validate the accuracy of the TEWC model against actual experimental data. The TEWC model demonstrated excellent agreement with the experimental results, as shown in Fig. 8(a). However, a slight difference was noted at 302 K and beyond 314 K. In these regions, simulation results were found to marginally overestimate the water generation at mentioned temperatures, which may be due to mesh element size or linear estimation of simulation. Fig. 8(b) shows the mid-plane temperature distribution surrounding the thermoelectric cold plate. Ambient air at 308 K and 80% RH enters the chamber and comes in contact with cold plate resulting in temperature reduction and condensation of water

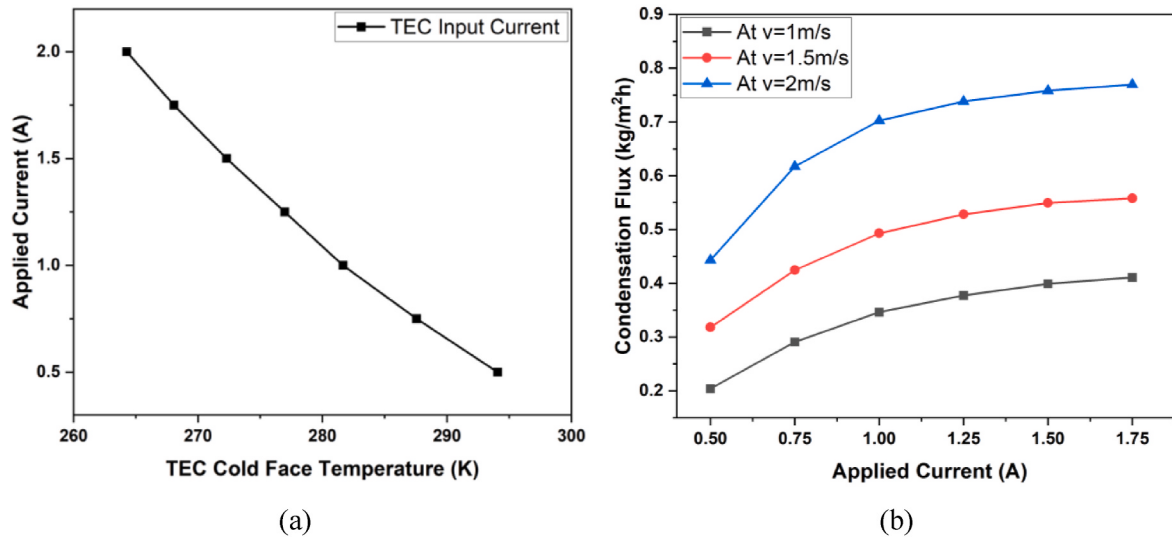


**Fig. 5.** (a) TEC cold face Temperature at different current input (b) Amount of water vapor condensation with varying current of TECs.

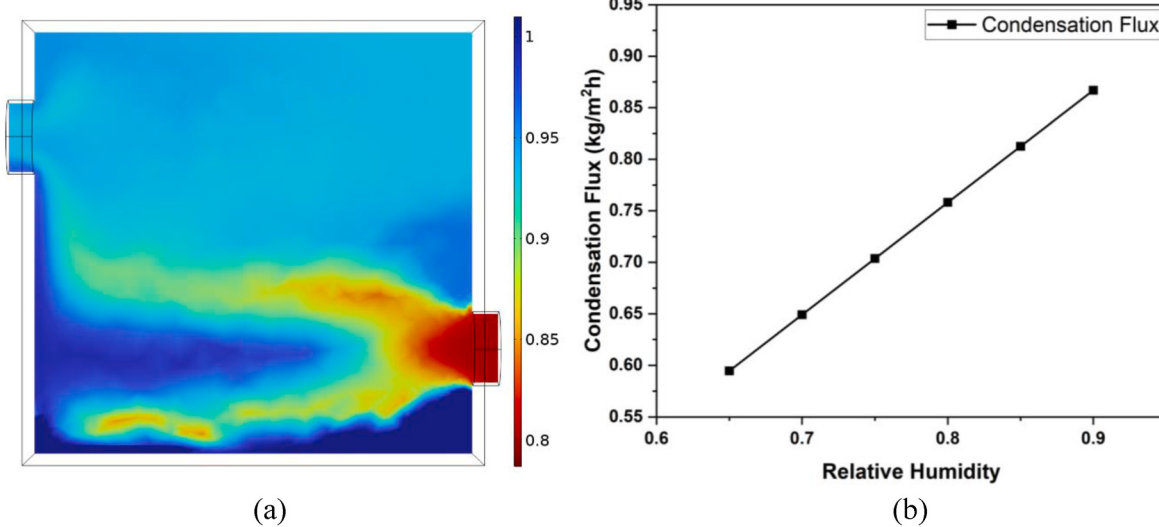


**Fig. 6.** (a) RH gradient of moist air domain at mid plane (b) Amount of water vapor condensation with varying RH.

vapors while exiting the chamber at 297 K. As expected, the temperature progressively decreases as we move closer to the cold plate (blue zone at the bottom) in a vertical downward direction. This temperature gradient is primarily driven by natural convection, where the difference in air density caused by the temperature variation creates a buoyant flow. This is because the boundary condition, the cold plate temperature, directly influences the overall temperature range within the system. Lowering the cold plate temperature results in a corresponding decrease in temperatures throughout the domain. Fig. 8(c) shows the variation of condensation rate against TEC cold face temperature at different inlet air flow rates. As depicted from the graph increasing cold face temperature decreases the condensation rate while increasing the inlet air flow rate results in increasing the condensation rate. Because a higher flow rate increases the moisture flow and hence the condensation rate. The normalized condensation rate reached a peak of 0.758 kg/(m<sup>2</sup>h) by reducing cold face temperature from 300 K to 272 K at a constant humidity of 80% and inlet air temperature of 308 K as shown in Fig. 8(c).

By analyzing the above factors, the computational study provides valuable insights into optimizing the design and operation of TEC-based water generation systems. This knowledge can help maximize water production while minimizing energy consumption.

### 3.1.5. TEWC system comparison

The productivity of the present TEWC system was compared with other AWG systems, such as solar chimney proposed by Wu et al. [16] and ammonia absorption refrigeration cycle-based AWG by Salek et al. [38]. As evidenced by the data in Table 4, the present TEWC system significantly outperformed other AWGs in terms of water yield under the same environmental conditions, highlighting the superior performance and potential benefits of the present system in challenging environments.

### 3.2. Analysis of AWE result

#### 3.2.1. I-V characteristics

I-V characteristics, showing the correlation between cell voltage and current density, serve as a crucial means of assessing an alkaline water electrolyzer's performance. Different factors influencing this curve were analyzed through computational analysis.

I-V characteristics of the present study were compared with experimental data of Rodríguez and Amores [23] in order to validate the model's electrochemical response. The model results showed excellent agreement with the experimental data, as illustrated in Fig. 9. However,

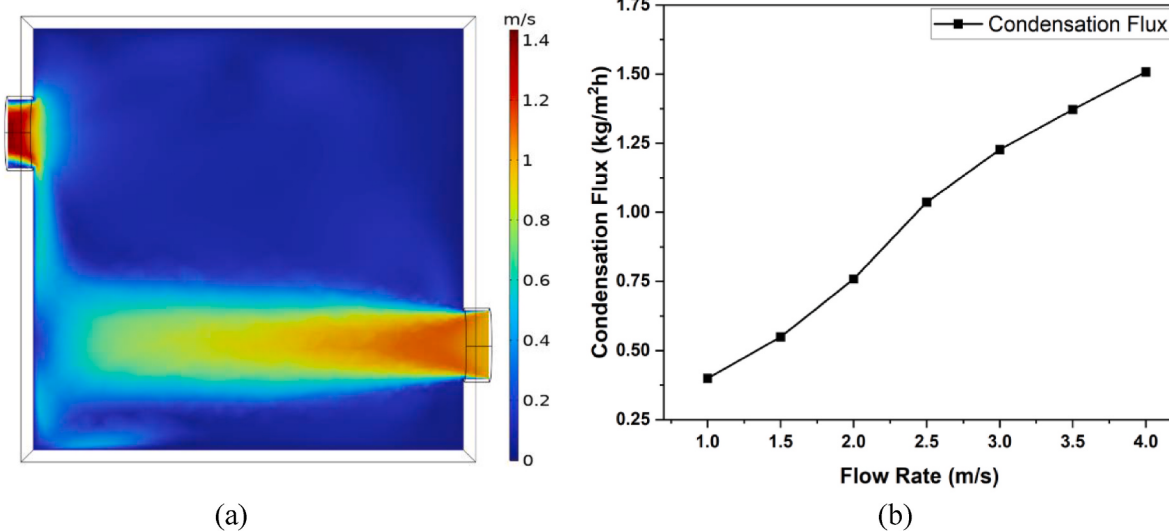


Fig. 7. (a) Velocity gradient of moist air domain at mid plane (b) Amount of water vapor condensation with varying Flow rate.

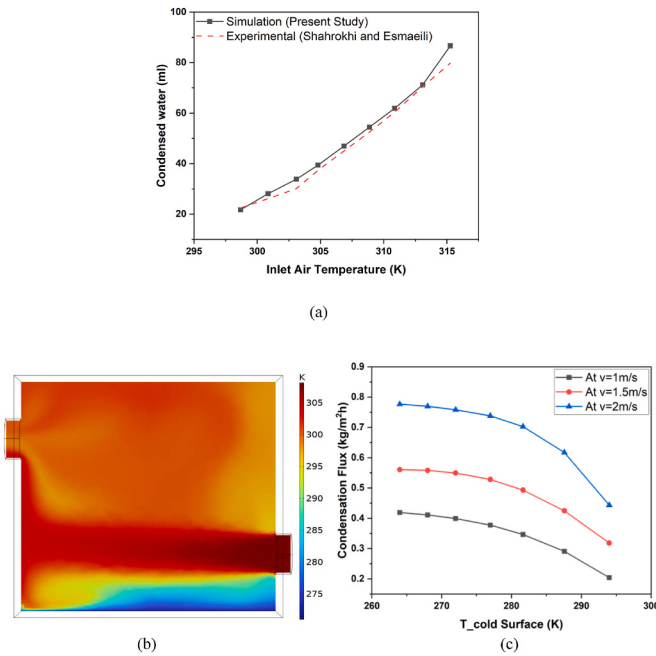


Fig. 8. (a) Amount of water condensed per hour with varying temperature of inlet Air  
(b) Temperature gradient of moist air domain at mid plane (c) Amount of water vapor condensation with varying Flow rate and TEC cold plate temperature.

Table 4  
Comparison of the AWG systems.

Systems	Water Yield (kg/(m <sup>2</sup> h))	Conditions
Present TEWC system	7.8	T = 35°C, RH = 80%
Solar chimney by Wu et al. [16]	6.8	T = 35°C, RH = 80%
AWG by Salek et al. [38]	7.2	T = 35°C, RH = 80%

a slight discrepancy was noted at low current densities, corresponding to lower voltages. In this region, activation overpotentials were found to dominate the energy required for electrolysis. In simpler terms, the limitations imposed by the slow rates of the cathode and anode reactions at these voltages were highlighted. This suggests that the electrokinetic

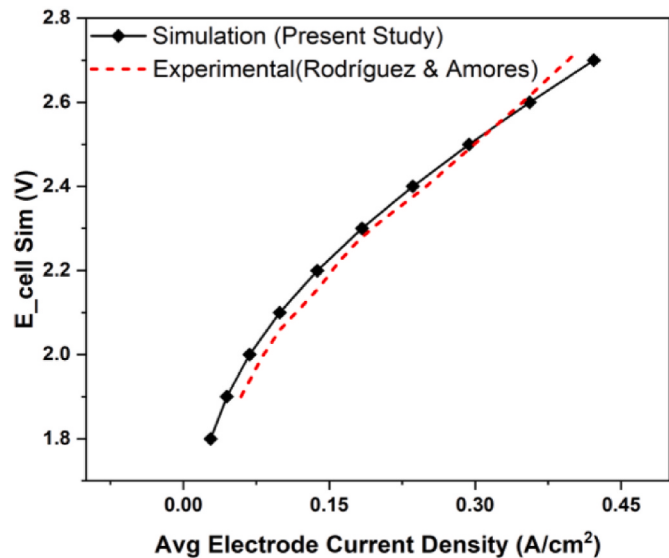


Fig. 9. I-V characteristics: simulation comparison with experimental cell voltage (model conditions: 343 K, 6 M KOH, and 1.5 m/s).

parameters are likely responsible for the difference between the model and real data. Two crucial electrokinetic parameters, exchange current density ( $i_0$ ) and charge transfer coefficient ( $\alpha$ ), are incorporated within the model. It is well-established that both parameters are highly sensitive to operating conditions such as temperature, pressure, and electrolyte flow rate [23]. While the influence of  $i_0$  on electrolysis has been extensively studied [26], the impact of  $\alpha$  has received less attention. Notably, in most literature the 0.5 value of  $\alpha$  is typically assigned to both reactions.

Temperature and reaction-dependent values were employed for  $i_0$  within this work (see Table 2). However, constant values for  $\alpha$  were used for both reduction and oxidation across all operating conditions. This reliance on approximations, rather than incorporating the actual value for each temperature, might explain the small deviations as shown in Fig. 9. However, instead of these slight discrepancies, the model exhibits a very low overall error and performs satisfactorily, as will be demonstrated in the following sections.

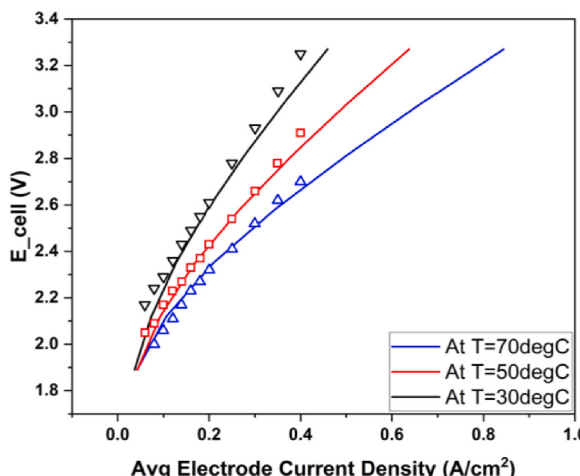
### 3.2.2. Influence of temperature

The temperature response of the present AWE model was compared with the experimental response of Rodríguez and Amores [23], as shown in Fig. 10(a). The model showed excellent agreement with experimental data. In Fig. 10(a), the impact of temperature on cell performance was analyzed and decrease in cell potential was measured to determine the specific advantages of operating at higher temperatures. As expected, the cell potential at a given current density declines with increasing temperature. Higher temperatures enhance reaction kinetics, lowering the reversible voltage and the required energy. This behavior has been previously reported by other researchers for AWE systems [15,18,19,21, 23]. Fig. 10(a) shows a significant drop in cell voltage, from 2.98 V at 303 K to 2.57 V at 343 K at a current density of  $0.34 \text{ A/cm}^2$ , which can be seen due to improved electrode kinetics at higher temperatures. This rise in cell temperature from 303 K to 343 K is responsible for a 16% reduction in overall cell voltage. And finally, Fig. 10(b) shows the relationship between cell potential and hydrogen evolution flux at different temperatures. As depicted from Fig. 10(b) hydrogen evolution rate increase with increasing cell temperature. It is because of higher temperatures reduce the reversible voltage that ultimately leads to higher  $\text{H}_2$  production rate at same potential.  $\text{H}_2$  evolution rate at cathode reached a maximum of  $5.2 \text{ kg}/(\text{m}^2\text{h})$  at 343 K,  $1.4 \text{ A/cm}^2$  and potential of 3.96 V.

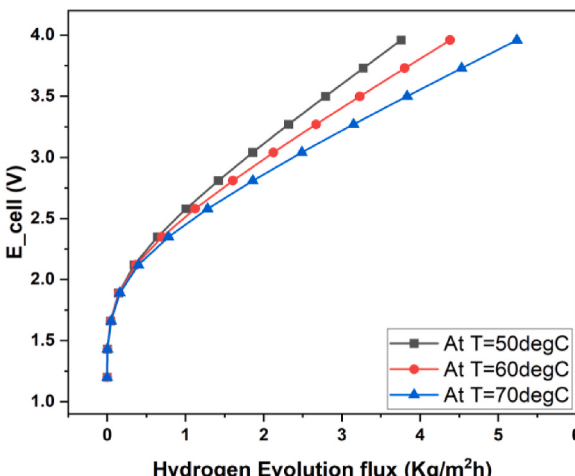
These findings offer valuable insights into the cell's performance during electrolysis. It is evidenced from Fig. 10(a) that the best correlation between experimental and calculated results occurs at 30 °C, 50 °C, and 70 °C which highlight the significant impact of temperature on cell performance.

### 3.2.3. Optimizing electrode-diaphragm gap in AWE cells

In AWE cell, the distance or gap between the electrode and the separator significantly impacts ohmic overpotential. A shorter distance reduces the amount of electrolyte separating these components, leading to lower ohmic resistance. However, excessively narrow cell gaps can trap gas bubbles during electrolysis, causing a rise in ohmic overpotential. Therefore, an ideal electrode-diaphragm spacing exists for optimal AWE cell performance. Researchers have explored this concept and calculated optimal distances in various studies. Fig. 11 illustrates the polarization curves at different electrode-diaphragm distances, with other parameters given in Table 2. The modeled curves show a slight decline as the gap decreases from 5 mm to 1.5 mm demonstrating that a reduced distance between the electrode and diaphragm lowers the electrolysis potential and increases current density.



(a)



(b)

**Fig. 10.** (a) I-V characteristics: Comparison of Model results shown as line with Experimental results shown as markers, (b)  $\text{H}_2$  evolution flux at  $\text{H}_2$  electrode (model conditions: 6 M KOH, 1 mm gap, and flowrate 1.5 m/s).

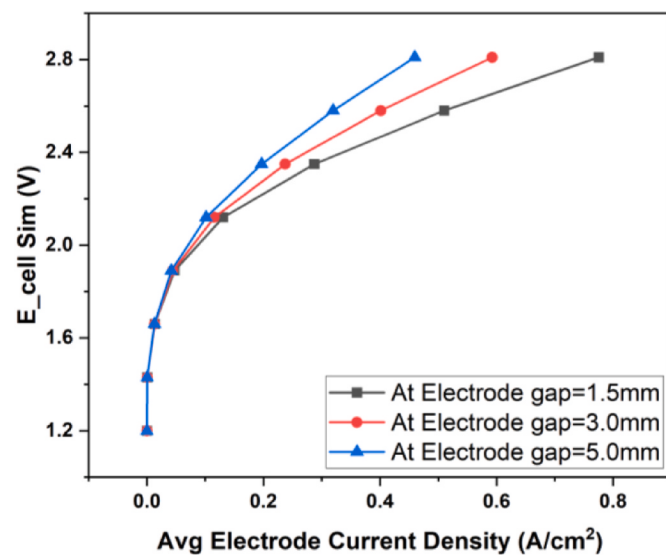


**Fig. 11.** I-V characteristics at different electrode-diaphragm gap (1.5–5 mm) (model conditions: 343 K, 6 M KOH).

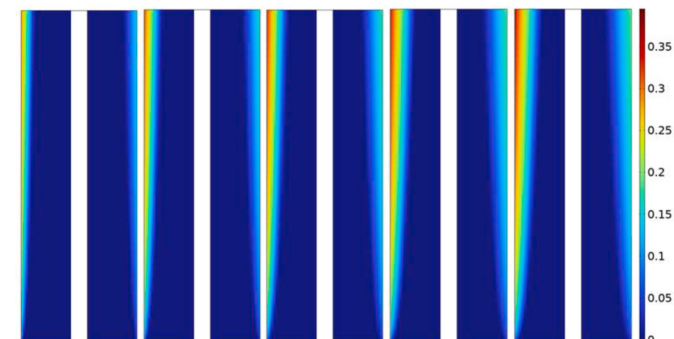
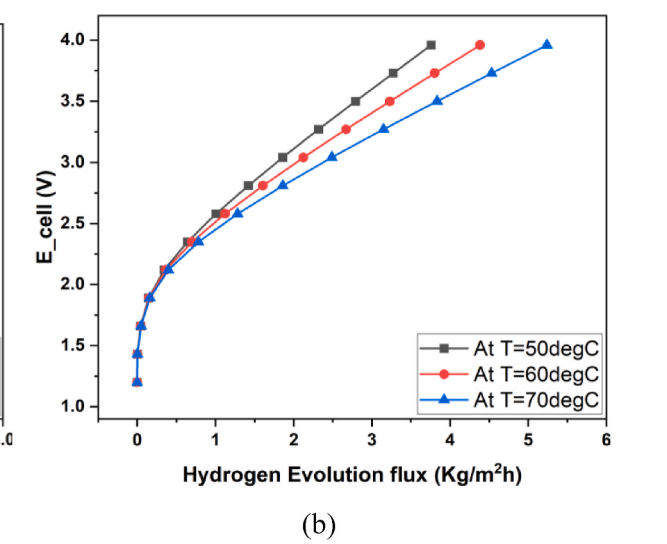


**Fig. 12.** Volume Fraction gradient at different current density values in  $\text{H}_2$  and  $\text{O}_2$  compartments (Boundary conditions: 343 K, 6 M KOH, and 1.5 m/s).



### 3.2.4. Gas generation profile

Fig. 12 shows the gas profile gradient at different current density. The void fractions (percentage of space occupied by gas bubbles) for hydrogen and oxygen exhibit a characteristic trend near the electrode surface. The observed trend indicates a gradual increase in void fraction from the bottom to the top of the electrode, caused by gas accumulation and flow rate effects. The hydrodynamic behavior of the two-phase flow system, comprising the gaseous and electrolyte phases, plays a crucial role in determining the performance characteristics of the AWE cell. The generated gas bubbles also play a crucial role. As they form, bubbles create a thickening curtain along the electrode surface in a vertical direction. This phenomenon induces turbulence, which enhances the mixing and distribution of participating species, ultimately improving mass transfer. The formation of gas bubbles can result in their adherence to the electrode surface, inhibiting some regions from participating in electrochemical reactions. This bubble adhesion phenomenon contributes to an increase in ohmic overpotential, demanding a higher energy input and subsequently impacting the overall performance of the cell.

## 4. Conclusion

This study employed computational analysis to investigate a novel system for green hydrogen production: a coupled system of TEWC for atmospheric water harvesting and AWE for hydrogen generation as a sustainable source in remote and arid regions. One significant hurdle for green hydrogen production is freshwater resources in remote and arid regions. To address geographical variations between renewable energy and freshwater resources. Computational analysis is carried out to study the performance of this coupling system and its behavior under different operating conditions. Critical parameters for the optimization of the overall system have been evaluated, by considering their effects on both the TEWC as well as AWE cell.

- After numerical investigation of TEWC, it was concluded that increasing the current input to TECs enhances their cooling efficiency, leading to a more effective condensation of water vapor. This highlights the TEWC system's ability to optimize water generation through precise control of the cooling process.
- Similarly higher relative humidity and flow rate of the inlet air significantly boosts condensation rates, resulting in increased water generation, while lowering these quantities limit the vapors availability leading to a reduced condensation rate.
- The TEWC model shows excellent agreement with experimental results, validating its accuracy in predicting water generation and showed that optimizing TEC cold face temperature, relative humidity, and inlet air flow rate can significantly enhance water generation. These findings provide valuable insights for improving system efficiency, maximizing water production while minimizing energy consumption.

I-V characteristics curve of AWE model was compared with experimental data to validate the model's electrochemical response. The results showed excellent agreement with the experimental data. This model excels in its adaptability to various operating conditions. It can analyze both fluid dynamics and electrochemical processes simultaneously. These capabilities make it a powerful and cost-effective design tool, ideal for optimizing cell efficiency and boosting green hydrogen production.

- The AWE model's response to variations in electrolysis parameters was assessed through I-V characteristics at different temperatures, electrode-diaphragm distances, and overpotentials. Both experimental and simulated data indicated that the electrolysis cell's performance improved with higher temperatures, shorter electrode-diaphragm distances, and lower overpotentials. Thus, the model

successfully captures the performance of the alkaline water electrolysis cell under various operating conditions.

- In addition to analyzing the electrochemical side, the model offers valuable insights into fluid dynamics. Simulations revealed that the generated gases form a "curtain effect" near the electrodes, increasing the gas volume fraction (void fraction) vertically as they accumulate. Furthermore, higher currents lead to more extensive gas distribution in the chamber. These findings offer valuable information for optimizing purposes.
- It was observed that the hydrogen evolution rate at the cathode reached a maximum of 5.2 kg/m<sup>2</sup>h during electrolysis process with 343 K, 3.96 V and with average electrode current density of 1.403 A/cm<sup>2</sup>.

## CRediT authorship contribution statement

**Hilal Ahmad:** Writing – original draft, Visualization, Methodology, Investigation. **Taqi Ahmad Cheema:** Writing – review & editing, Supervision, Conceptualization. **Hadeed Ahmed Sher:** Validation, Formal analysis, Data curation. **Cheol Woo Park:** Software, Resources, Project administration, Funding acquisition.

## Declaration of competing interest

On behalf of all authors, I confirm that this work is original and has not been published before nor is currently under consideration for publication elsewhere. Moreover, all the authors involved are aware of this submission and agree with the contents of the manuscript.

I hereby declare that there is no conflict of interest of any kind involved for this submission.

## Acknowledgments

This study was supported by a National Research Foundation of Korea (NRF) grant funded by the Korea government (MSIP) (No. RS-2023-00208673).

## References

- [1] Veziroglu TN, Barbir F. Solar-hydrogen energy system : the choice of the future. Environ Conserv 1991;18(4):304–12. <https://doi.org/10.1017/s0376892900022554>.
- [2] Armaroli N, Balzani V. Solar electricity and solar fuels: status and perspectives in the context of the energy transition. Chem Eur J 2016;22(1):32–57. <https://doi.org/10.1002/chem.201503580>.
- [3] Guo Y, Li G, Zhou J, Liu Y. Comparison between hydrogen production by alkaline water electrolysis and hydrogen production by PEM electrolysis. IOP Conference Series: Earth Environ 2019;371(4):042022. <https://doi.org/10.1088/1755-1315/371/4/042022>.
- [4] Cattani L, Cattani P, Magrini A, Figoni R, Dondi D, Vadivel D. Suitability and energy sustainability of atmospheric water generation Technology for green hydrogen production. Energies 2023;16(18):6440. <https://doi.org/10.3390/en16186440>.
- [5] Liu S, He W, Hu D, Lv S, Chen D, Wu X, Xu F, Li S. Experimental analysis of a portable atmospheric water generator by thermoelectric cooling method. Energy Proc 2017;142:1609–14. <https://doi.org/10.1016/j.egypro.2017.12.538>.
- [6] Summers M, Asiabpour B. Improving heat transfer from peltier devices used in an atmospheric water generation. Intern J Eng Mater Manuf 2021;6(3):170–5. <https://doi.org/10.26776/ijemm.06.03.2021.08>.
- [7] Sanaye S, Shourabi A, Borzuei D. Sustainable water production with an innovative thermoelectric-based atmospheric water harvesting system. Energy Rep 2023;10: 1339–55. <https://doi.org/10.1016/j.egyr.2023.07.062>.
- [8] Shahrokh F, Esmaeili A. Optimizing relative humidity based on the heat transfer terms of the thermoelectric atmospheric water generator (AWG): innovative design. Alex Eng J 2023;67:143–52. <https://doi.org/10.1016/j.aej.2022.09.003>.
- [9] Joel J, Zafar HR, Jobin F, James A, Tharian MG, Mathew J. Design and optimization of an atmospheric water generator using thermoelectric cooling modules. Mater Today Proc 2021. <https://doi.org/10.1016/j.mtpr.2021.09.149>.
- [10] Shafeian N, Ranjbar AA, Gorji TB. Progress in atmospheric water generation systems: a review. Renewable Sustainable Energy Rev 2022;161:112325. <https://doi.org/10.1016/j.rser.2022.112325>.
- [11] Esfe MH, Esfandeh S, Toghraie D. Numerical simulation of water production from humid air for Khuzestan province: investigation of the Peltier effect (thermoelectric

- cooling system) on water production rate. *Case Stud Therm Eng* 2021;28:101473. <https://doi.org/10.1016/j.csite.2021.101473>.
- [12] Joshi VP, Joshi VS, Kothari HA, Mahajan MD, Chaudhari MB, Sant KD. Experimental investigations on a portable fresh water generator using a thermoelectric cooler. *Energy Proc* 2017;109:161–6. <https://doi.org/10.1016/j.egypro.2017.03.085>.
- [13] Alenezi A, Jung HH, Alabaidly Y. Experimental and numerical analysis of an atmospheric water harvester using a thermoelectric cooler. *Atmosphere* 2023;14 (2):276.
- [14] Eslami M, Tajeddini F, Etaati N. Thermal analysis and optimization of a system for water harvesting from humid air using thermoelectric coolers. *Energy Convers Manag* 2018;174:417–29.
- [15] Kashiba BA, Kashiba CB. The solar cyclone: a solar chimney for harvesting atmospheric water. *Energy* 2008;33(2):331–9. <https://doi.org/10.1016/j.energy.2007.06.003>.
- [16] Wu Y, Ming T, De Richter R, Höffer R, Niemann HJ. Large-scale freshwater generation from the humid air using the modified solar chimney. *Renew Energy* 2020;146:1325–36. <https://doi.org/10.1016/j.renene.2019.07.061>.
- [17] Jang D, Choi W, Cho HS, Cho WC, Kim CH, Kang S. Numerical modeling and analysis of the temperature effect on the performance of an alkaline water electrolysis system. *J Power Sources* 2021;506:230106. <https://doi.org/10.1016/j.jpowsour.2021.230106>.
- [18] Bideau DL, Mandin P, Benbouzid M, Kim M, Sellier M, Ganci F, Inguanta R. Eulerian two-fluid model of alkaline water electrolysis for hydrogen production. *Energies* 2020;13(13):3394. <https://doi.org/10.3390/en13133394>.
- [19] Wong XY, Zhuo Y, Shen Y. Numerical analysis of hydrogen bubble behavior in a zero-gap alkaline water electrolyzer flow channel. *Ind Eng Chem Res* 2021;60(33): 12429–46. <https://doi.org/10.1021/acs.iecr.1c02554>.
- [20] Brauns J, Schönebeck J, Kraglund MR, Aili D, Hnat J, Zitka J, Mues W, Jensen JO, Bouzek K, Turek T. Evaluation of diaphragms and membranes as separators for alkaline water electrolysis. *J Electrochem Soc* 2021;168(1):014510. <https://doi.org/10.1149/1945-7111/abda57>.
- [21] Niroula S, Chaudhary C, Subedi A, Thapa BS. Parametric modelling and optimization of alkaline electrolyzer for the production of green hydrogen. *IOP Conf Ser Mater Sci Eng* 2023;1279(1):012005. <https://doi.org/10.1088/1757-899X/1279/1/012005>.
- [22] Lee J, Alam A, Ju H. Multidimensional and transient modeling of an alkaline water electrolysis cell. *Int J Hydrogen Energy* 2021;46(26):13678–90. <https://doi.org/10.1016/j.ijhydene.2020.10.133>.
- [23] Rodríguez J, Amores E. CFD modeling and experimental validation of an alkaline water electrolysis cell for hydrogen production. *Processes* 2020;8(12):1634. <https://doi.org/10.3390/pr8121634>.
- [24] Zarghami A, Deen NG, Vreman AW. CFD modeling of multiphase flow in an alkaline water electrolyzer. *Chem Eng Sci* 2020;227:115926. <https://doi.org/10.1016/j.ces.2020.115926>.
- [25] Barco-Burgos J, Eicker U, Saldaña-Robles N, Saldaña-Robles AL, Alcántar-Camarena V. Thermal characterization of an alkaline electrolysis cell for hydrogen production at atmospheric pressure. *Fuel* 2020;276:117910. <https://doi.org/10.1016/j.fuel.2020.117910>.
- [26] Lopata J, Kang Z, Young J, Bender G, Weidner JW, Cho H-S, Shimpalee S. Resolving anodic current and temperature distributions in a polymer electrolyte membrane water electrolysis cell using a pseudo-two-phase computational fluid dynamics model. *J Electrochim Soc* 2021;168(5):054518. <https://doi.org/10.1149/1945-7111/abfe7b>.
- [27] Abdelsalam E, Almomani F, Kafiah F, Alnawafah H, Juaidi A, Abdallah R. Integrating solar chimney power plant with electrolysis station for green hydrogen production: a promising technique. *Int J Hydrogen Energy* 2024;52:1550–63. <https://doi.org/10.1016/j.ijhydene.2023.08.305>.
- [28] Abdelsalam E, Almomani F, Alnawafah H, Habash D, Jamjoum M. Sustainable production of green hydrogen, electricity, and desalinated water via a Hybrid Solar Chimney Power Plant (HSCPP) water-splitting process. *Int J Hydrogen Energy* 2024;52:1356–69. <https://doi.org/10.1016/j.ijhydene.2023.06.165>.
- [29] Arthur T, Millar GJ, Love J. Integration of waste heat recovered from water electrolysis to desalinate feedwater with membrane distillation. *J Water Proc Eng* 2023;56:104426. <https://doi.org/10.1016/j.jwpe.2023.104426>.
- [30] Harada H, Sinha A, Yajima T, Kawajiri Y. Model-based techno-economic analysis of an integrated synthetic natural gas production system with direct air capture and water electrolysis. *Carbon Capture Sci Techno* 2024;10:100181. <https://doi.org/10.1016/j.ccst.2023.100181>.
- [31] Modestino MA, Dumortier M, Hosseini Hashemi SM, Haussener S, Moser C, Psaltis D. Vapor-fed microfluidic hydrogen generator. *Lab Chip* 2015;15(10): 2287–96. <https://doi.org/10.1039/C5LC00259A>.
- [32] Wendt HP. *Electrochemical hydrogen technologies: electrochemical production and combustion of hydrogen*. 1990.
- [33] Incropera FP, Dewitt DP, Bergman TL, Lavine AS. *Fundamentals of heat and mass transfer*. sixth ed. John Wiley & Sons; 2007.
- [34] Çengel YA, Ghajar AJ. *Heat and mass transfer – fundamentals and applications*. fifth ed. McGraw-Hill; 2015.
- [35] Bideau DL, Mandin P, Benbouzid M, Kim M, Sellier M, Ganci F, Inguanta R. Eulerian two-fluid model of alkaline water electrolysis for hydrogen production. *Energies* 2020;13:3394.
- [36] Godula-Jopek A. *Hydrogen production: electrolysis*. Wiley-VCH Verlag GmbH & Co. KGaA; 2015.
- [37] Jain S, Sikarwar BS, Muralidhar K. Improved heat transfer modeling of moist air condensation on hydrophobic metallic surface. *Heat Tran Eng* 2023;1–19. <https://doi.org/10.1080/01457632.2023.2275237>.
- [38] Salek F, Moghaddam AN, Naserian MM. Thermodynamic analysis and improvement of a novel solar driven atmospheric water generator. *Energy Convers Manag* 2018;161:104–11. <https://doi.org/10.1016/j.enconman.2018.01.066>.